PNAS
www.pnas.org

Supplementary Information for

Imaging the Renner-Teller effect using laser-induced electron diffraction

Kasra Amini, Michele Sclafani, Tobias Steinle, A.T. Le, Aurelien Sanchez, Carolin Müller, Johannes Steinmetzer, Lun Yue, José Ramón Martínez Saavedra, Michaël Hemmer, Maciej Lewenstein, Robert Moshammer, Thomas Pfeifer, Michael G. Pullen, Joachim Ullrich, Benjamin Wolter, Robert Moszynski, F. Javier García de Abajo, C.D. Lin, Stefanie Gräfe, Jens Biegert

Jens Biegert
Email: jens.biegert@icfo.eu

This PDF file includes:

Supplementary Information Text

A. Experimental Description. We generate high-energy rescattering electron wave packets by making use of a home-built optical parametric chirped pulse amplifier (OPCPA) set-up that generates 85 fs (FWHM), 3.1 μm pulses at a 160 kHz repetition rate with up to 21 W output power (1, 2). The OPCPA system is seeded by a passively carrier-envelope-phase (CEP) stable frequency comb generated by the difference frequency of a dual-colour fibre laser system (3). The mid-infrared wavelength of 3.1 μm here used ensures that the target is strong-field ionised in the tunneling regime. The laser pulse is focused to a spot size of 6−7 μm (1/e^2 waist) resulting in a peak intensity of 9×10^{13} Wcm^{-2}. At this peak intensity, the Keldysh parameter was γ = 0.30 with a ponderomotive energy of U_p = 85 eV. As the average energy of the returning electron wave packet scales quadratically with the driving wavelength, this laser source allows us to generate electrons with maximum classical return and backscattered electron energies of $E_{ret,max} = 3.17U_p \approx 270$ eV and $E_{back,max} = 10U_p \approx 850$ eV, respectively.

We measure the full three-dimensional momentum distribution of the photoelectrons in coincidence with the CS_2^+ ion using a reaction microscope (ReMi) - for details, see for example Ref. (4). Briefly, a doubly-skimmed supersonic jet of carbon disulfide provides the cold molecular target with a rotational temperature of <100K. Homogeneous electric and magnetic extraction fields are employed to guide the ionic fragments and the corresponding electrons to separate detectors in the ReMi. Each detector consists of delay line detectors (Roentdek), which record the full three-dimensional momenta of charged particles from a single molecular fragmentation event in full electron-ion coincidence. In all experiments, the laser polarisation is aligned perpendicular to the spectrometer axis, parallel to the jet. A thorough description of the experimental advantages offered by the unique combination of our mid-IR OPCPA with a ReMi to investigate strong-field physics in the quasistatic regime is provided in Ref. (5). Nevertheless, it is worth emphasizing that our electron-ion coincidence experimental setup allows the structural retrieval of neutral CS_2 through its cation CS_2^+ since the geometrical structure of CS_2 to be investigated does not significantly change upon ionization.

B. Extraction Of Molecular Structure. Structural information of the molecular sample is retrieved from the electron momentum distribution within the frame of the quantitative rescattering theory (QRS) and the independent atomic-rescattering model (IAM) (6–8). The procedure for molecular structure extraction has been explained in detail previously (9,10), with only a brief discussion given here. Molecular structural information is extracted from our LIED measurement through the best chi-square fit of the experimental molecular contrast factor (MCF), γ^e, to the theoretical MCF, γ^t, using

$$\chi^2(R_{CS}, \Phi_{SCS}) = \sum_n \left[\gamma^e(k_r, \theta_{r,n}) - \gamma^t(k_r, \theta_{r,n})\right]^2 \quad \text{(S1)}$$

where (k_r, θ_r) represent the momentum and the scattering angle of the rescattered electron in the rescattering frame (see Fig. 1*A*), whilst *n* is the index of the discretized scattering angle.

The theoretical MCF is calculated using the independent atomic-rescattering model (IAM), and is given by

$$\gamma^{t}(k_r, \theta_r) \equiv \frac{\langle I_{tot}\rangle(\theta) - \langle I_A\rangle(\theta_r)}{\langle I_A\rangle(\theta_r)} = \frac{\sum_{i\neq j} f_i f_j^* \int e^{i\vec{q}\cdot\vec{R}_{ij}} N(\Omega_L)\rho(\Omega_L)d\Omega_L}{\sum_i |f_i|^2 \int N(\Omega_L)\rho(\Omega_L)d\Omega_L}. \quad \text{(S2)}$$

Here, I_{tot} is the total scattering cross-section that we measure, and I_A is the incoherent sum of the scaterring cross-sections from all atoms within the molecule, given by

$$\langle I_A\rangle(\theta) = \sum_i |f_i|^2 \int N(\Omega_L)\rho(\Omega_L)d\Omega_L\,, \quad \text{(S3)}$$

where Ω_L is the alignment angle of the molecule relative to the polarization axis of the laser field, $\rho(\Omega_L)$ is the molecular alignment distribution, $N(\Omega_L)$ is the ionization rate, and f_i is the complex scattering amplitude for the i^{th} atom by the incident electron. Whilst $\langle I_{tot}\rangle(\theta) - \langle I_A\rangle(\theta_r)$ is the molecular interference term, $\langle I_M\rangle(\theta)$. In fact, the phase factor in $\langle I_M\rangle(\theta)$ encodes both the scattering angle of the incident electron, as quantified by the momentum transfer

$$\vec{q} = \vec{k}_r - \vec{k}_{r0},$$

as well as the internuclear distance vector $\vec{R}_{ij} = \vec{R}_i - \vec{R}_j$ between atoms *i* and *j*. Therefore, the MCF provides a sensitive measure of $\vec{R}_{ij}$ in molecules (9, 10).

The experimental MCF is given by

$$\gamma^{e}(k_r, \theta_r) \equiv \frac{\langle I^{e}_{tot}\rangle(\theta_r) - \langle I_A\rangle(\theta_r)}{\langle I_A\rangle(\theta_r)} = \frac{\beta D^{e}(\theta_r) - \langle I_A\rangle(\theta_r)}{\langle I_A\rangle(\theta_r)}, \quad \text{(S5)}$$

and is calculated using the experimentally determined differential cross-section (DCS), $D_e(\theta_r)$, which is weighted by a factor β that provides the best fit to the theoretical MCF.

Here, the molecular alignment distribution, $\rho(\Omega_L)$, was assumed to be isotropic. We calculated the ionization rate, $N(\Omega_L)$, using the strong-field approximation (SFA) and the time-dependent density-functional theory (TDDFT) method, and we consider contributions from the highest occupied molecular orbital (HOMO) only. The contribution of lower lying states (HOMO-1 or HOMO-2) is several orders of magnitude smaller than from the HOMO and hence can be neglected (11). Furthermore, non-perturbative TDDFT for 0.8 μm light (12) and our own real-time-real-space TDDFT calculations for 3.1 μm simulations have shown that the ionization of the inner $3\sigma_u$ orbital (HOMO-2) of CS_2 only becomes the dominant response to the laser field for intensities larger than 3×10^{15} Wcm^{-2} and molecules whose molecular axis is aligned with the field (12). It should also

be noted that we found the MCFs (shown in Fig. 1*B*) to be quite insensitive with respect to small changes in the ionization rates and molecular alignment distribution.

In CS_2, the IAM has been shown to yield excellent agreement between experimental and theoretical DCSs for electrons with kinetic energies of 100−200 eV and scattering angles in the 20−135° range (13). In the present measurements, we record rescattered electrons with sufficient statistics in the kinetic energy range of 160−180 eV and an angular interval of 50−120° (*i.e.*, well within the range of validity of the IAM approximation). The MCF has been shown to be a very sensitive metric for imaging the molecular structure of diatomic and small molecules (10,14–16). At a fixed returning energy, the C-S bond length, R_{CS}, is sampled in the retrieval procedure from 1.5 Å to 2.5 Å, whereas the S-C-S angle, Φ_{SCS}, is explored from the linear structure (Φ_{SCS} = 180°) to a strongly bent structure (Φ_{SCS} = 60°). As shown in Fig. 1*B*, MCFs are used for retrieving R_{CS} and Φ_{SCS} by comparing the experimental and theoretical MCFs.

The theoretical MCFs providing the best agreement with the experimental data are shown by the red trace in Fig. 1*B*. The MCF associated with the equilibrium geometric structure of the $\widetilde{X}^1\Sigma_g^+$ electronic ground state is also shown (orange). Complete χ^2 maps calculated according to Eq. *S1* are shown in Fig. 1*C*. We measure a C-S bond length R_{CS} = 1.86 $\pm$ 0.23 Å and an S-C-S angle Φ_{SCS} = 104.0 $\pm$ 20.2°, which correspond to CS_2 in the bent geometry in the presence of the intense laser field, as shown in Fig. 2.

C. TDDFT Calculations. In order to model the interaction of CS_2 with the intense, mid-infrared laser fields, real-time-real-space TDDFT calculations have been performed using the Octopus (17) program package. A cartesian grid has been utilized with an equidistant grid spacing of dx = dy = dz = 0.12 Å. For computational feasibility, the grid size was reduced to a sphere with a radius of 8.47 Å. Afterwards, absorbing boundary conditions were employed in order to avoid grid reflections of the free components of the electron wave function. With this procedure, the molecule is well situated in the grid and direct ionization can be modelled. However, effects due to electron recollision, such as recollisional excitation or ionization, are not included. Due to the large wave packet spreading at these long wavelengths, we expect these effects to be minor. The laser field was modelled by a sin^2 envelope with a central wavelength of 3100 nm, a duration of approximately 8 optical cycles FWHM (*i.e.,* 85 fs) and a peak intensity of 9×10^{13} Wcm^{-2}.

Exchange contributions were described via the LDA_X functional (18, 19), while correlation was modelled by a modified Perdew-Zunger LDA functional (20). LDA is commonly employed to model strong-field interaction with molecules due to its simplicity and lower computational cost. However, self-interactions do not cancel and its asymptotic behavior scales wrongly. We corrected for self-interaction *via* the average density formalism (21). Table *S1* shows the converged ground state eigenenergies with different approaches and functionals. When comparing the eigenenergies calculated with different LDA functionals, the LDA_X by Perdew and Zunger (20) gave the best results compared to

experiment. Our results agree well with similar TDDFT-based results (12). As expected, the Hartree-Fock (HF) energies are overestimates of the experimental values, while the LDA functional in DFT underestimates the ionization potentials substantially due to the known wrong asymptotic behavior originating from the self-interaction (12).

Our TDDFT calculations have been employed in order to get an overview over the excitation and ionization dynamics of CS_2 in an intense laser field. We have implemented the calculations of the orbital norms, $\langle \psi_i(t) | \psi_i(t) \rangle$, and auto-correlation functions, $\langle \psi_i(t=0) | \psi_i(t) \rangle$, in the Octopus program suite (17) in order to be able to investigate which Kohn-Sham molecular orbitals interact with the mid-infrared laser pulse depending on the relative orientation of the laser polarization axis to the molecular axis. Calculations have been performed for θ = 0° and 90°, where θ is the angle of the laser polarization relative to the molecular axis.

We have performed two different types of calculations, one keeping the nuclei frozen throughout the calculations, and another one with moving nuclei (Ehrenfest dynamics). Our (non-perturbative) TDDFT calculations show that, for the pulse parameters employed in the experiment, mainly the π_g (non-bonding orbital, *n*) and π_u (bonding orbital) orbitals are depopulated, depending on the orientation (angle θ). This is in agreement with earlier calculations by Bandrauk *et al.* at 800 nm (12).

Additionally, the TDDFT calculations using (classically) moving nuclei within the Ehrenfest approach show that during laser interaction, the system stretches symmetrically and bends (from R_{CS} = 1.56 Å and Φ_{SCS} = 180° to R_{CS} = 1.64 Å and Φ_{SCS} = 124.1°, for θ = 90°, see Fig. *S1*). For θ = 0°, also small contributions of an asymmetric stretch dynamics can be gathered from the TDDFT calculations (Fig. *S2*). However, contributions from the asymmetric stretch are minor when taking orientation-averaging into account. From the TDDFT calculations, we thus extract the transition to the first excited state ($n \rightarrow \pi_u^*$) to be the dominant excitation channel, the dynamics of which will be examined in more detail with wave packet methods, as described below.

D. Quantum Chemistry Calculations. The singlet electronic ground and excited state potential surfaces, $V_i(R, \Phi)$, as well as the (transition) dipole moments, $\vec{\mu}(R, \Phi)$, of both the neutral CS_2 and the cation CS_2^+ have been calculated using the OpenMolcas 8.0 program suite (23) at the state-averaged CASSCF(12,10)/cc-pVTZ level of theory[24]. For the neutral molecule, a (12,10) space was chosen, with the active orbitals displayed in Fig. *S3*.

For the cation, the corresponding (11,10) space was chosen. Altogether, the first 10 configuration interaction (CI) roots have been calculated, using C_1 symmetry. The molecule is arranged such that at linear geometries the molecular axis is the y-axis; the bent molecule lies in the xy-plane.The lowest four singlet potential energy surfaces, S_0 – S_3, and representative cuts along the surfaces (see Fig. 1*B*) are shown in Figs. *S4* – *S5*. The lowest doublet potential curves of the cation are shown in Fig. *S6*.

Analysis of the transition dipole moments shows that the transition to the lowest (S_1, $\widetilde{A}^1A_2$) electronic state is strictly forbidden at all geometries (including symmetrically stretched and bent configurations), while the transition to the S_2 ($\widetilde{B}^1B_2$) electronic state is forbidden at linear geometries but (weakly) allowed at bent and symmetrically stretched geometries. We therefore consider for our quantum dynamical calculations only the ground (S_0, $\widetilde{X}^1\Sigma_g^+$) and the second excited (S_2, $\widetilde{B}^1B_2$) electronic states, the corresponding permanent dipole moments of these electronic states and the transition dipole moment coupling them.

From these results, we already conclude that at 180° (linear geometry), no transition to any of the lower-lying excited electronic states can occur. However, the transition only becomes possible if the molecule bends and stretches, enabling a transition to only this particular S_2 electronic state (*i.e.*, our $\widetilde{B}^1B_2$ state).

E. Quantum Dynamical Wave Packet Calculations. Dynamics calculations have been performed by numerically integrating the time-dependent Schrödinger equation on a 1024×512 grid (in R and Φ) for the two Born-Oppenheimer electronic surfaces $\widetilde{X}^1\Sigma_g^+$ and $\widetilde{B}^1B_2$, coupled *via* dipole interaction:

$$i\hbar\frac{\partial}{\partial t}\begin{pmatrix}\chi_{\widetilde{X}}(R,\Phi,t)\\ \chi_{\widetilde{B}}(R,\Phi,t)\end{pmatrix} = \left[\begin{pmatrix}\hat{T}0\\ 0\hat{T}\end{pmatrix} + \begin{pmatrix}V_{\widetilde{X}}(R,\Phi) - \vec{\mu}_{\widetilde{X}}(R,\Phi)\vec{E}(t) & -\vec{\mu}_{\widetilde{X}\to\widetilde{B}}(R,\Phi)\vec{E}(t)\\ -\vec{\mu}_{\widetilde{X}\to\widetilde{B}}(R,\Phi)\vec{E}(t) & V_{\widetilde{B}}(R,\Phi) - \vec{\mu}_{\widetilde{B}}(R,\Phi)\vec{E}(t)\end{pmatrix}\right]\begin{pmatrix}\chi_{\widetilde{X}}(R,\Phi,t)\\ \chi_{\widetilde{B}}(R,\Phi,t)\end{pmatrix}. \tag{S6}$$

In the above equation, $\hat{T}$ is the kinetic energy operator, given by

$$\hat{T} = \left(\frac{\rho_R^2}{2M_{CS}} + \frac{\rho_\Phi^2}{2M_{SCS}}\right), \tag{S7}$$

with a mass M_{CS} = 13.3142 amu used for stretching and M_{SCS} = 31.9721 amu for the bending motion. By doing so, we neglect the small dependence of the mass M_{SCS} on the bending angle Φ. The time-dependent nuclear wave functions $\chi_i(R,\Phi,t)$ describe the field-driven vibrational wave packet dynamics in the electronic states i = $\widetilde{X}$, $\widetilde{B}$. We account for the relative orientation of the molecule relative to the laser polarization direction through the angle θ, defined such that

$$\tan\theta = \frac{\mu_y}{\mu_x}, \tag{S8}$$

for molecules lying in the xy-plane. The laser field, $E(t)$, is described classically as

$$E(t) = E_0 f(t - t_c)\cos(\omega t), \tag{S9}$$

where E_0 is the laser field strength, $f(t - t_c)$ is the Gaussian envelope function centered around t_c, and ω is the laser frequency. For these quantum dynamical calculations, we use the split-operator method (25), while the Fourier transform is done numerically using the FFTW3 library (26). In order to avoid grid reflections, absorbing boundary conditions are employed along the C-S stretching coordinate R_{CS}.

We have performed three different calculations for θ = 0°, 45° and 90°. Our wave packet calculations of the neutral CS_2 molecule show that upon interaction with the intense laser field, the electronic ground state, $\widetilde{X}^1\Sigma_g^+$, of the CS_2 molecule is strongly re-shaped (see Fig. 3*A*). Consequently, the field-free vibrational ground state is not an eigenstate of the field-dressed potential curve, as the potential is modified in the field. Thus, a vibrational wave packet is formed, and the molecule in its electronic ground state starts to slightly stretch to approximately R_{CS} = 1.7 Å and then begins to bend up to 170° (see Fig. 4*A*).

Then, almost transiently, a small amount of population is transferred to the $\widetilde{B}^1B_2$ excited state, which immediately starts to propagate on the field-dressed potential energy surface of the $\widetilde{B}^1B_2$ state (Figs. 3*A* and 3*B*). As to be expected when considering the transition dipole moments and their components, the transition for 0° (along the y-axis, which is the molecular axis, see above) is largest, while the out-of-plane transition (along the z-axis) is negligible. These quantum dynamical calculations show that the wave packet in the excited state bends up to about 120° at around the peak of the laser pulse envelope (*i.e. t* = 0 fs in Fig. 4*A*) where the field is strongest, and thus, the tunneling rate reaches a maximum. As we cannot properly describe ionization with the quantum dynamical calculations (transition dipole moments from the neutral to the cation are not accounted for here), we separately calculate the dynamics of the cation.

For the cation, we have performed field-free Born-Oppenheimer-type calculations on a few lowest-lying potential energy surfaces in order to estimate the dynamical timescales imprinted during the excursion of the liberated electron until its return (within ∼8 fs), when it diffracts against the cation. The results are shown in Fig. 4*B*. We conclude that in all of the eight lowest-lying states considered, an initially stretched and bent neutral CS_2 can, in the time interval between ionization and probing by the returning LIED electron 8 fs later, further stretch and bend by $\Delta R_{CS} \approx 0.1$ Å and $\Delta\Phi_{SCS} \approx 10°$, depending on the electronic state of the cation CS_2^+ that is populated.

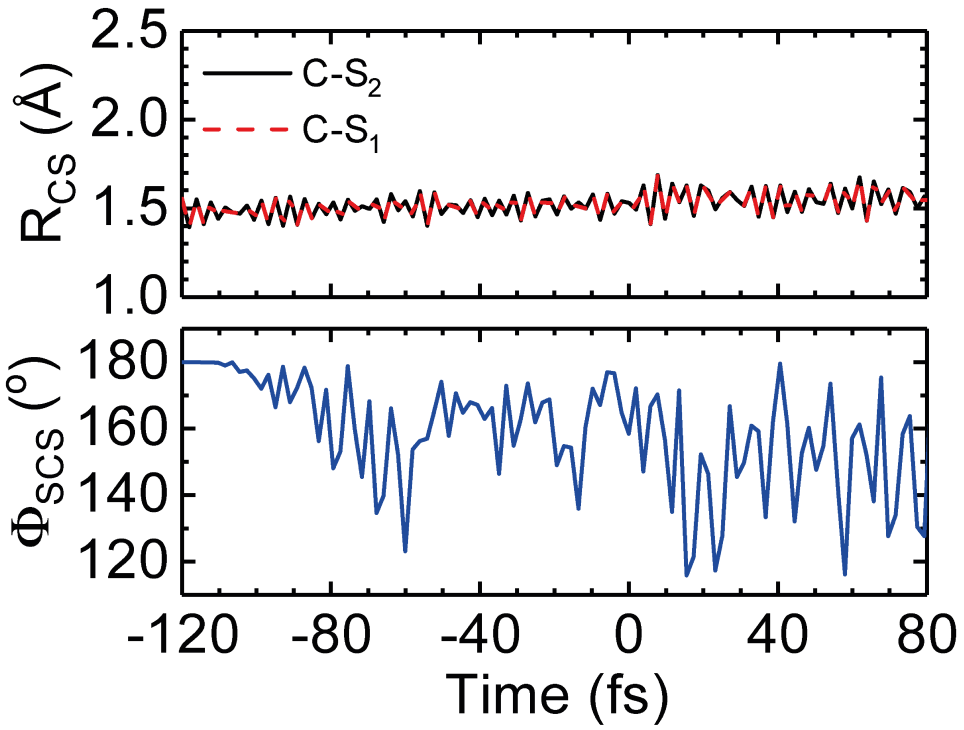

Fig. S1 | Nuclear dynamics of CS_2 in the presence of a 3.1 μm laser field. Time-dependent coordinate expectation values of the individual C-S bond lengths (*Top*), R_{CS}, and the S-C-S bending angle (*Bottom*), Φ_{SCS}, as extracted from our real-time, real-space TDDFT calculations with moving nuclei within the Ehrenfest approach. The case for perpendicular orientation of the laser polarization axis relative to the molecular axis (θ = 90°) is shown. The same laser parameters as in the LIED measurement are used. Symmetric stretching motion mainly occurs accompanied by strong deviations from the linear geometry. Here, t = 0 fs corresponds to the peak of the 85 fs (FWHM) 3.1 μm pulse envelope.

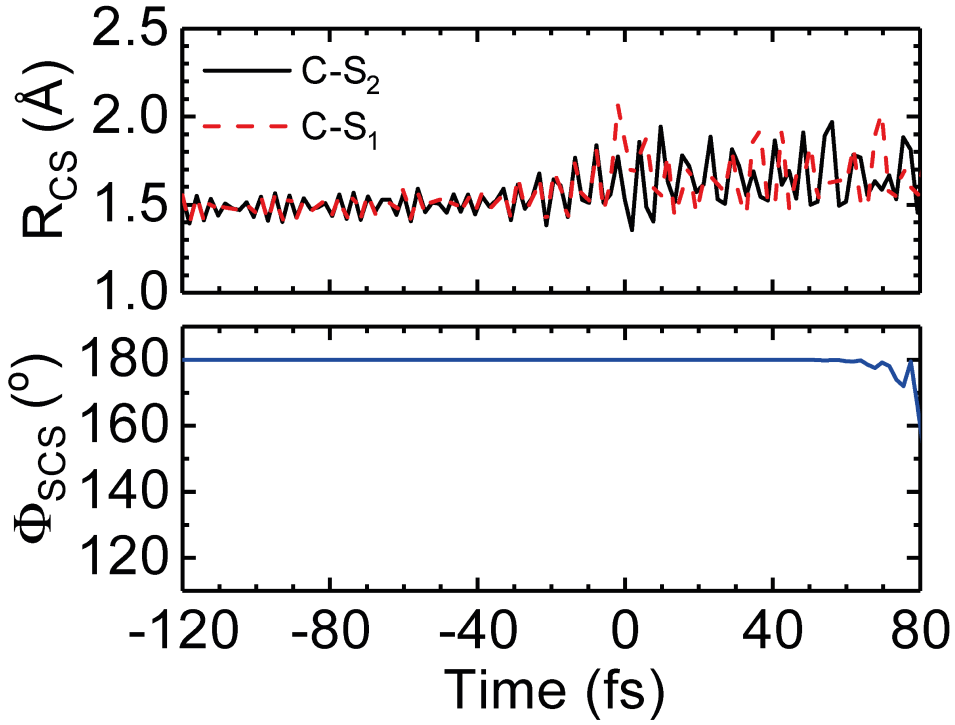

Fig. S2 | Nuclear dynamics of CS_2 in the presence of a 3.1 μm laser field. Same as in Figure *S1*, but for parallel orientation of the laser polarization axis relative to the molecular axis ($\theta = 0°$). For times $t < 0$ fs, mostly symmetric stretching dynamics can be observed, while for $t > 0$ fs antisymmetric stretching motion dominates.

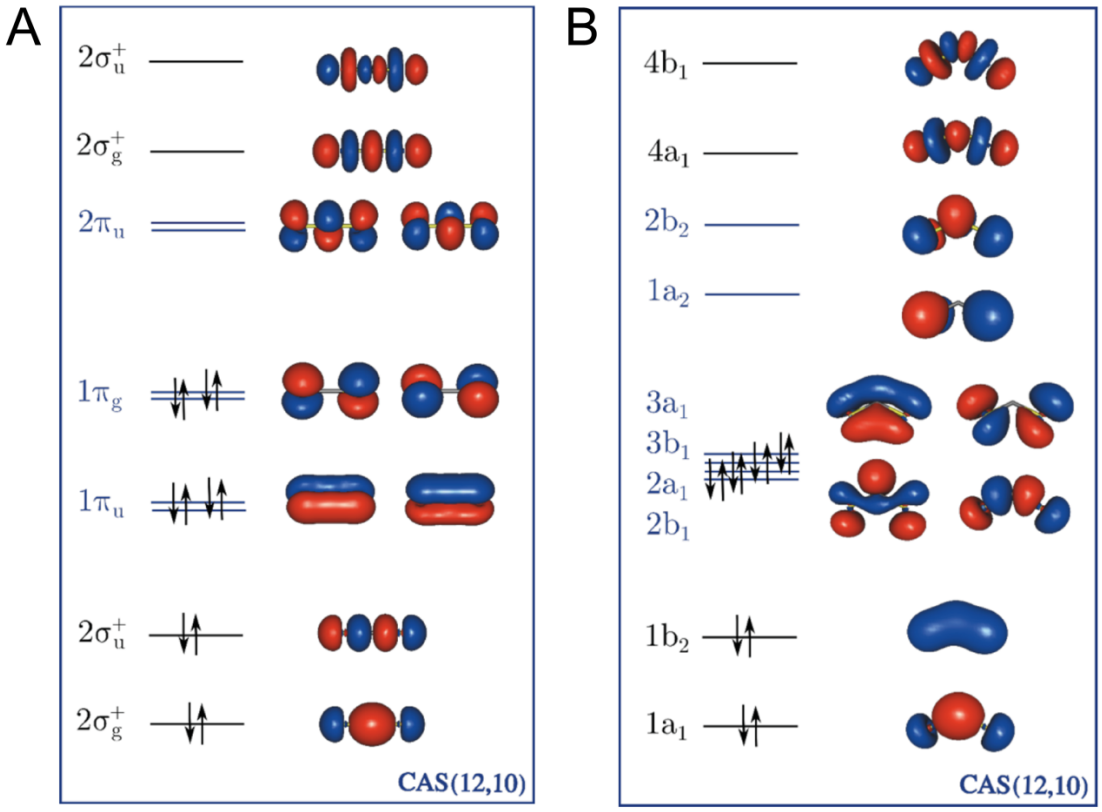

Fig. S3 | Molecular orbitals of neutral CS_2. (A) linear and (B) bent geometries chosen for the active space, showing the corresponding symmetry levels. We use a CAS(12,10)/cc-pVTZ level of theory within the OpenMolcas 8.0 program suite (23).

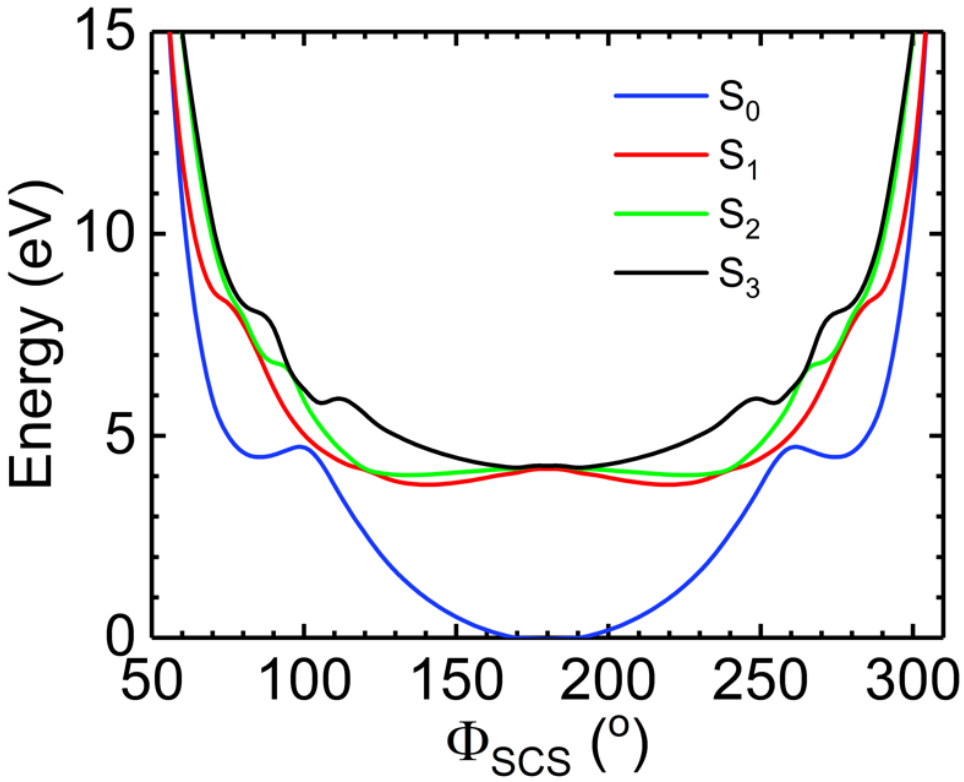

Fig. S4 | Potential energy curves of neutral CS_2 along SCS bond angle coordinate. Cut along the field-free potential energy surfaces of neutral CS_2 at the equilibrium C-S internuclear distance of the ground electronic state, R_{CS} = 1.6 Å, showing the potential energy curves as a function of the SCS angle, Φ_{SCS}, for the lowest four singlet electronic states (see labels).

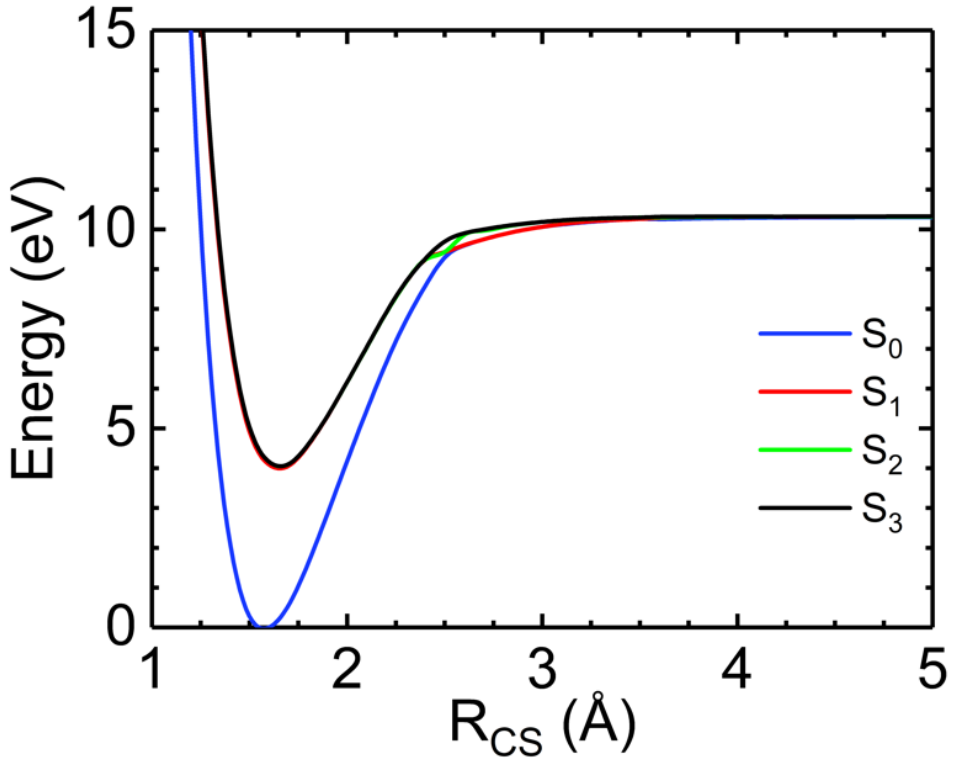

Fig. S5 | Potential energy curves of neutral CS_2 along C-S internuclear distance coordinate. Cut along the field-free potential energy surfaces of neutral CS_2 at the equilibrium SCS angle Φ_{SCS} = 180° showing the potential energy curves as a function of the C-S internuclear distance R_{CS} of the symmetric stretch mode for the lowest four singlet electronic singlet states (see labels).

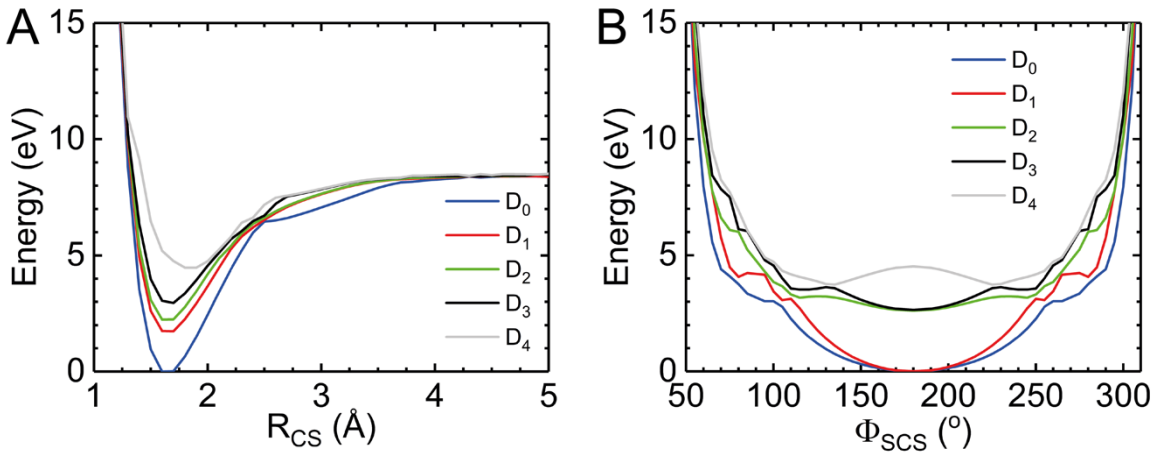

Fig. S6 | Potential energy curves of the CS_2^+ cation. (A) Cuts along the PESs of CS_2^+ cation at the equilibrium SCS angle Φ_{SCS} = 180° showing the potential energy curves as a function of the C-S internuclear distance R_{CS} along the symmetric stretch mode. (B) Cuts along the PESs at the equilibrium C-S internuclear distance of the electronic ground state, R_{CS} = 1.6 Å, showing the potential energy curves as a function of the SCS angle, Φ_{SCS}, for the lowest five doublet electronic states (see labels).

Table S1 | Field-free eigenenergies of the highest molecular orbitals (MOs) of CS_2 with the real-time-real-space TDDFT as implemented in the Octopus program package (17). The energies are given in electronvolts (eV). Displayed are the results of different calculations with different functionals and self-interaction corrections, as labelled. The experimental values are taken from Eland *et al.* (22). The grey shaded LDA (adsic) calculations gave the best eigenenergies as compared to the experimental values and were the ones chosen for the following calculations when interaction with the field is included.

MO	HF	LDA	LDA (amaldi)	LDA (adsic)	LB94 (adsic)	LB94	LB94 (amaldi)	Expt.[22] (adsic)
$2\sigma_g$	-31.2	-21.4	-29.0	-24.9	-25.7	-33.7	-25.3	-
$2\sigma_u$	-27.9	-19.3	-26.9	-22.8	-23.5	-31.4	-23.1	-
$2\sigma_g$	-18.5	-12.7	-19.9	-15.9	-17.2	-24.8	-16.3	-
$2\sigma_u$	-15.9	-10.8	-18.0	-14.0	-15.1	-22.8	-14.4	-14.5
$1\pi_g$	-14.4	-9.8	-17.0	-13.9	-14.5	-22.2	-13.9	-12.7
$1\pi_g$	-10.2	-6.9	-13.9	-10.3	-11.5	-19.1	-10.8	-10.1

References

1. Baudisch M, Wolter B, Pullen M, Hemmer M, Biegert J (2016) High power multi-color OPCPA source with simultaneous femtosecond deep-UV to mid-IR outputs. *Opt Lett* 41:3583-3586.

2. Elu U, *et al.* (2017) High average power and single-cycle pulses from a mid-IR optical parametric chirped pulse amplifier. *Optica* 4: 1024-1029.

3. Thai A, Hemmer M, Bates P, Chalus O, Biegert J (2011) Sub-250-mrad, passively carrier–envelope-phase-stable mid-infrared OPCPA source at high repetition rate. *Opt Lett* 36:3918-3920.

4. Ullrich J, *et al.* (2003) Recoil-ion and electron momentum spectroscopy: reaction-microscopes. *Rep Prog Phys* 66:1463.

5. Wolter B, *et al.* (2015) Strong-field physics with mid-IR fields. *Phys Rev X* 5:021034.

6. Morishita T, Le A-T, Chen Z, Lin CD (2008) Accurate retrieval of structural information from laser-induced photoelectron and high-order harmonic spectra by few-cycle laser pulses. *Phys Rev Lett* 100:013903.

7. Chen Z, Le A-T, Morishita T, Lin CD (2009) Quantitative rescattering theory for laser-induced high-energy plateau photoelectron spectra. *Phys Rev A* 79:033409.

8. Lin CD, Le A-T, Chen Z, Morishita T, Lucchese R (2010) Strong-field rescattering physics–self-imaging of a molecule by its own electrons. *J Phys B* 43:122001.

9. Xu J, Chen Z, Le A-T, Lin CD (2010) Self-imaging of molecules from diffraction spectra by laser-induced rescattering electrons. *Phys Rev A* 82:033403.

10. Pullen MG, *et al.* (2015) Imaging an aligned polyatomic molecule with laser-induced electron diffraction. *Nat Commun* 6:7262.

11. Kumarappan V, *et al.* (2008) Multiphoton electron angular distributions from laser-aligned CS_2 molecules. *Phys Rev Lett* 100:093006.

12. Bandrauk AD, Fowe EP (2010) Non perturbative time-dependent density functional theory, TDDFT: Study of ionization and harmonic generation in linear di-(N_2) and tri-(CO_2, OCS, CS_2) atomic molecules with ultrashort intense laser pulses-orientational effects. *Coherence and Ultrashort Pulse Laser Emission*.

13. Murai H, *et al.* (2013) A comprehensive and comparative study of elastic electron scattering from OCS and CS_2 in the energy region from 1.2 to 200 eV. *J Chem Phys* 138:054302.

14. Blaga CI, *et al.* (2012) Imaging ultrafastmolecular dynamicswith laser-induced electron diffraction. *Nature* 483:194.

15. Pullen MG, *et al.* (2016) Influence of orbital symmetry on diffraction imaging with rescattering electron wave packets. *Natu Commun* 7:11922.

16. Wolter B, *et al.* (2016) Ultrafast electron diffraction imaging of bond breaking in di-ionized acetylene. *Science* 354:308.

17. Andrade X, *et al.* (2015) Real-space grids and the octopus code as tools for the development of new simulation approaches for electronic systems. *Phys Chem Chem Phys* 17:31371.

18. Dirac PA (1930) Note on exchange phenomena in the Thomas atom. *Math Proc Camb Philos Soc* 26:376.

19. Bloch MF (1929) Bemerkung zur Elektronentheorie des Ferromagnetismus und der elektrischen Leitfähigkeit. *Zeitschrift für Physik* 57:545.

20. Perdew JP, Zunger A (1981) Self-interaction correction to density-functional approximations for many-electron systems. *Phys Rev B* 23:5048.

21. Legrand C, Suraud E, Reinhard P (2002) Comparison of self-interaction-corrections for metal clusters. *J Phys B* 35:1115.

22. Eland JH, Danby C (1968) Photoelectron spectra and ionic structure of carbon dioxide, carbon disulphide and sulphur dioxide. *Int J Mass Spectrom* 1:111.

23. Aquilante F, *et al.* (2016) Molcas 8: New capabilities for multiconfigurational quantum chemical calculations across the periodic table. *J Comput Chem* 37:506.

24. Woon DE, Dunning Jr TH (1995) Gaussian basis sets for use in correlated molecular calculations. V. Core-valence basis sets for boron through neon. *J Chem Phys* 103:4572.

25. Feit M, Fleck Jr J, Steiger A (1982) Solution of the schrödinger equation by a spectral method. *J Comput Phys* 47:412.

26. Frigo M, Johnson SG (1998) FFTW. *ICASSP conference proceedings* 3:1381.